Investigations of the domain structure of anisotropic sintered Nd–Fe–B-based permanent magnets

Witold Szmaja*

Department of Solid State Physics, University of Łódź, Pomorska 149/153, 90-236 Łódź, Poland

Abstract

The magnetic structure of anisotropic sintered Nd–Fe–B-based permanent magnets of different chemical compositions has been studied by the conventional Bitter pattern technique, the colloid-scanning electron microscopy (SEM) method, magnetic force microscopy (MFM) and the type-I magnetic contrast of SEM. The methods used have been digitally enhanced. Improvements over earlier results have been achieved. In the thermally demagnetized state, practically each grain consists of magnetic domains. At the surface perpendicular to the alignment axis, the main domains forming a maze pattern of typically 1–2 μm in width and surface reverse spikes of typically 0.5–1 μm in diameter are present. This coarse domain structure resembles those for sufficiently thick uniaxial crystals with strong magnetocrystalline anisotropy, commonly reported in earlier studies. Nevertheless, besides the coarse domain structure, fine surface domains having widths in the range 20–250 nm are observed by MFM. The fine scale domains are found to be magnetized perpendicular to the specimen surface and their existence is attributed to the reduction of the magnetostatic energy near the surface. The main and surface domain widths, the domain wall energies, the domain wall thicknesses, the single-domain particle diameters and the exchange constants for the investigated magnets were determined. The influence of Dy addition on the magnetic domain structure was estimated. As predicted by the theory, the main and surface domain widths were observed to increase with increasing Dy concentration. Studies of the magnetic structure during magnetizing cycle, carried out on the surface parallel to the alignment axis, show that the domain walls are easily moved within the grains and that the magnetization reversal occurs predominantly by the nucleation and expansion of reverse domains at structural imperfections near the grain boundaries. Some aspects related to magnetic domain observation by the methods used are also discussed.

1. Introduction

Permanent magnets are used in a wide range of applications and the market for them is continuing to expand as their magnetic characteristics and cost effectiveness are improved. The applications include actuators (loudspeakers, microphones, moving-coil meters, print-head actuators, disk-drive head actuators, actuators for industrial robots, pneumatic pumps and car door locks), motors (stepper motors, brushless DC motors, DC servomotors), magnetic and electromagnetic separators, magnetic sensors, magnetic resonance imaging, microwave power tubes, generators, wigglers, magnetic water and oil treatment, and many others [1].

Among all permanent magnets, Nd–Fe–B-based magnets are currently the most powerful ones, with the highest available magnetic energies. They are produced in bulk form by two principal routes: (i) sintering microcrystalline powder into high energy, fully dense components; and (ii) melt quenching nanocrystalline material for use in bonded and hot deformed components. Generally, sintered magnets have high-energy products (30–50 MGOe), full density and relatively simple shapes. Bonded magnets have

*Tel.: +48 42 6355687; Fax: +48 42 6790030.

E-mail address: szmaja@mvii.uni.lodz.pl (W. Szmaja).

intermediate energy products (10–18 MGOe), lower density and can be formed into intricate net-shapes. Hot deformed magnets possess full density, intermediate to high-energy products (15–46 MGOe), isotropic or anisotropic properties and have the potential to be formed into net shapes [2].

A detailed knowledge and complete understanding of the magnetic microstructure are not only of fundamental interest, but also of technological significance. In particular, they are very important for the development of high-performance permanent magnets. In this context, the knowledge of the magnetic domain behavior in relation to the macroscopic parameters and physical microstructure of the magnets is also significant for theoretical modeling of their magnetic properties. The magnetic domain structure of Nd–Fe–B-based specimens was extensively investigated in the past, using far-field magneto-optic Kerr microscopy [3–11], the conventional Bitter pattern technique [6,12–14] and transmission electron microscopy (TEM) [15–18]. And more recently, it was also observed with magnetic force microscopy (MFM) [19–22].

The high performance of Nd–Fe–B-based permanent magnets is due to a high saturation magnetization and a strong uniaxial magnetocrystalline anisotropy of the tetragonal $Nd_2Fe_{14}B$ phase (and more generally, the $Nd_2Fe_{14}B$ phase modified by small additions of other elements, usually Dy substitution for Nd and/or Co substitution for Fe), which is the main hard magnetic phase in these magnets. Besides the $Nd_2Fe_{14}B$ matrix phase, sintered Nd–Fe–B-based magnets contain minor phases such as Nd-rich phase, $NdFe_4B_4$ phase, α-Fe, Nd oxides and pores. The minor phases are generally found to occur at the grain boundaries of the matrix phase or at grain junctions [7,16,23–25].

The purpose of this paper is to investigate the domain structure of sintered Nd–Fe–B-based permanent magnets of different chemical compositions. To obtain useful complementary information, the magnetic structure was observed by different methods, including the Bitter colloid technique with the use of an optical microscope and a scanning electron microscope (SEM), MFM and the type-I magnetic contrast of SEM. The methods were supported by digital image recording, enhancement and analysis. In most cases, this allowed to obtain domain images which have high contrast and show the details clearly, and to analyze them in detail. Improvements over earlier results

were achieved. The domain images presented in this paper are the original digital ones (i.e. obtained directly from the optical microscope, SEM or MFM) after application of a simple digital procedure for contrast improvement only, except where otherwise stated. The procedure used is described in detail in Ref. [26]. However, we wish to note here that this procedure does not modify the original intensities of the image points, but only changes the way of displaying the image on the computer monitor.

The Bitter pattern technique consists in depositing fine magnetic particles on the specimen surface. In the conventional (or classic) Bitter pattern method, a wet colloid and a conventional optical microscope are used [27], while in the colloid-SEM method a dried colloid and an SEM are used [28]. For a review of the Bitter pattern technique, see Ref. [29]. MFM utilizes the magnetostatic interaction between the specimen and a magnetic probe placed at a constant height (typically 10–200 nm) over the specimen surface. For reviews of the MFM method, see Refs. [30,31]. The type-I magnetic contrast in an SEM is due to the Lorentz deflection of secondary electrons by the stray fields above the specimen surface [32]. For a recent review of type-I magnetic contrast, see Ref. [33].

2. Experimental

The specimens studied were anisotropic sintered Nd–Fe–B-based magnets of different chemical compositions in the shape of cuboids a few millimeters in size, produced by powder metallurgy followed by sintering in an applied magnetic field. They consisted of large grains with an average size of about 10 μm, oriented with their *c*-axis, being the easy axis of magnetization, along the direction of the applied field. The magnetic properties of the specimens at room temperature are given in Table 1; the parameter of the relative magnetic anisotropy Q is defined as $Q = K/K_d$, i.e. it is the ratio of the (effective) magnetic anisotropy constant K to the stray field energy constant $K_d = 2\pi M_s^2$ (M_s is the saturation magnetization). The specimens denoted by A, B and C were obtained from NEOMAX Co., Ltd., while the specimens denoted by D were obtained from Vacuumschmelze GmbH & Co. KG.

The magnetic structure was investigated on the surfaces both perpendicular and parallel to the alignment axis. The observed surfaces were carefully polished to reduce the

Table 1
Magnetic properties of the studied Nd–Fe–B-based magnets

Specimen	Chemical composition	M_s (G)	$_MH_c$ (kOe)	$(BH)_{max}$ (MGOe)	H_a (kOe)	K (erg/cm^3)	Q
A	$Nd_{14.5}Fe_{79}B_{6.5}$	1130	10.1	48	65.1	3.7×10^7	4.6
B	$(Nd_{0.85}Dy_{0.15})_{14.5}Fe_{79}B_{6.5}$	1003	>21.0	38	84.3	4.2×10^7	6.7
C	$(Nd_{0.7}Dy_{0.3})_{14.5}Fe_{79}B_{6.5}$	907	>30.0	32	103.0	4.7×10^7	9.1
D	$Nd_{13.7}Dy_{0.2}Fe_{79.7}TM_{0.4}B_6$, where TM: Al, Ga, Co, Cu	1170	12.7	53	87.0	5.1×10^7	5.9

M_s is the saturation magnetization, $_MH_c$ is the intrinsic coercivity, $(BH)_{max}$ is the maximum energy density, H_a is the anisotropy field, K is the magnetocrystalline anisotropy constant, $Q = K/2\pi M_s^2$ is the relative magnetic anisotropy.

topographic contrast and thus effectively enhance the magnetic domain contrast. We used successively finer SiC abrasive papers (down to 1200 grade) and diamond powders (3, 1 and 0.25 μm in average diameter) with a water-free lubricant. In this respect, it should be noted that polishing Nd–Fe–B-based permanent magnets presents a difficulty because of the fact that they are multiphase, also mechanically anisotropic and have high hardness, and some intergranular constituents are chemically very reactive [20,23].

The magnetic structure was observed with the conventional Bitter pattern method, the colloid-SEM technique, MFM and the SEM type-I magnetic contrast. For each of the methods used, experimental conditions concerning investigation of the domain structure were optimized to improve the magnetic contrast in the images. In particular, digital image processing systems were applied to the original images for their enhancement and analysis. The digital systems used and their capabilities are described in detail in Refs. [26,34].

To study the domain structure by the Bitter pattern technique, a drop of water-based colloidal suspension of magnetite (Fe_3O_4) particles was applied to the specimen surface and covered with a thin microscope cover glass to spread the colloid uniformly on the surface. The optimum concentration of the colloid was determined experimentally. The domain patterns were observed using reflected unpolarized light under a metallographic microscope PZO MET-3 operated in the brightfield mode. For the purpose of studying the domain behavior under the influence of an external magnetic field parallel to the alignment axis of a permanent magnet, an electromagnet was used. The maximum value of the applied field was about 5 kOe. The domain structure in the thermally demagnetized state was also investigated with the colloid-SEM method using a Tesla BS 340 SEM, after previous drying the colloid placed on the specimen surface. To prevent charging of the specimen surface in the SEM, it was coated by sputtering a 15 nm thick layer of copper.

MFM measurements of the magnets in the thermally demagnetized state were carried out by an NT-MDT instrument operated in the AC (called also dynamic) mode using MikroMasch silicon cantilevers with tips magnetized along the tip axis, which was perpendicular to the specimen surface. In this case, MFM senses the vertical component of the derivative of the force between the specimen and the tip [30]. The image signal was detected as the phase or amplitude shift of an oscillating cantilever. The tips used were coated with a Co film of about 60 nm in thickness, onto which a Cr protective film of about 20 nm in thickness was deposited. The coercivity of the tips was approximately 400 Oe. All the MFM images shown in this paper were collected with a tip–specimen separation of 100 nm.

Investigations of the domain structure in the demagnetized state by the type-I magnetic contrast were made with the use of a Tesla BS 340 SEM with conventional tungsten filament and an Everhart–Thornley electron detector.

Images were taken using an electron beam with energy 20 keV and a maximum current of about 10 nA. The specimen tilt by 25° away from the detector was used to enhance the type-I magnetic contrast by filtering out the backscattered electrons and the higher energy secondary electrons. A circular aperture was placed in front of the scintillator Faraday cage of the detector for further enhancement of the magnetic contrast.

3. Results and discussion

3.1. Study of the domain structure in the thermally demagnetized state on the surface perpendicular to the alignment axis

Figs. 1 and 2 present typical images of the domain structure in the thermally demagnetized state on the surface perpendicular to the alignment axis, recorded by the conventional Bitter pattern and colloid-SEM methods, respectively. In both these figures, the domain patterns for specimens B (Figs. 1a and 2a) and D (Figs. 1b and 2b) are shown, for the purpose of more direct comparison. The domains of opposite magnetization (along the alignment axis) are displayed as dark and bright. The domain structure is composed of the main domains (which extend through the whole grain thickness and form a maze pattern) and surface domains of reverse magnetization (most frequently termed reverse domains or reverse spikes), the latter visible approximately as circles within the main domains. However, for all the specimens A–D studied, the main domains in images taken with the conventional Bitter pattern technique were noticeably larger than those in images recorded by the colloid-SEM method (compare Fig. 1a with Fig. 2a, and Fig. 1b with Fig. 2b); they had widths typically in the ranges 3–6 and 1–2 μm, respectively. In other words, this means that the main domains were not resolved in images obtained by the former technique. The described effect was already reported in Ref. [35]. The reason for this effect does not appear to be related to a limited optical resolution of typically 0.5 μm; the statement is additionally supported by the observation that reverse spike domains of about 0.5–1 μm in size were present in images taken by the conventional Bitter pattern technique (cf. Fig. 1). The reason is found to be related to different probing distances (i.e. the distance from the specimen surface to which the stray field of the specimen is effectively probed by magnetic particles of the colloid) for the two considered methods of domain observation. The conventional Bitter pattern technique is found to have a probing distance of about 0.5–1 μm [36,37], while in the case of the colloid-SEM method it seems to be reasonable to assume that its probing distance is about 0.1–0.3 μm. As a consequence, apart from the fact that the colloid-SEM method uses an SEM instead of a conventional optical microscope, this method is considerably more surface sensitive and clearly resolves domains, in contrast to the conventional Bitter pattern technique. The colloid-SEM
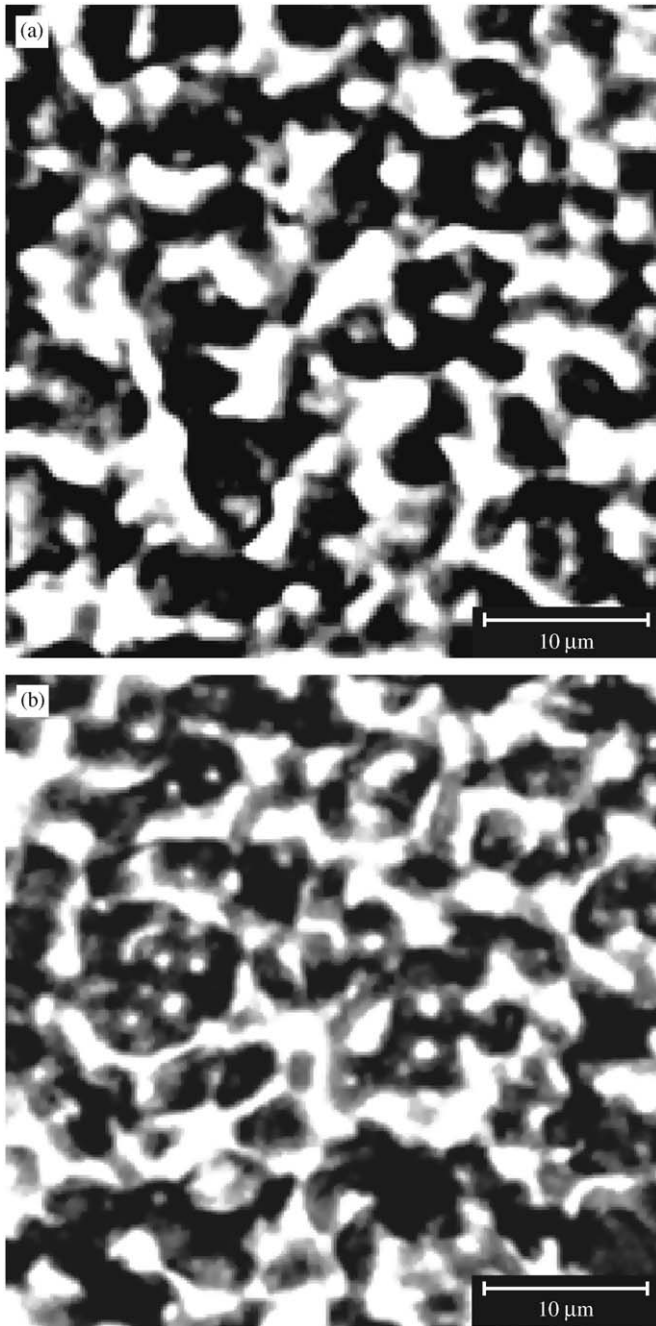
Fig. 1. Domain structure of specimens B (a) and D (b) in the thermally demagnetized state on the surface perpendicular to the alignment axis, made visible with the conventional Bitter pattern technique.
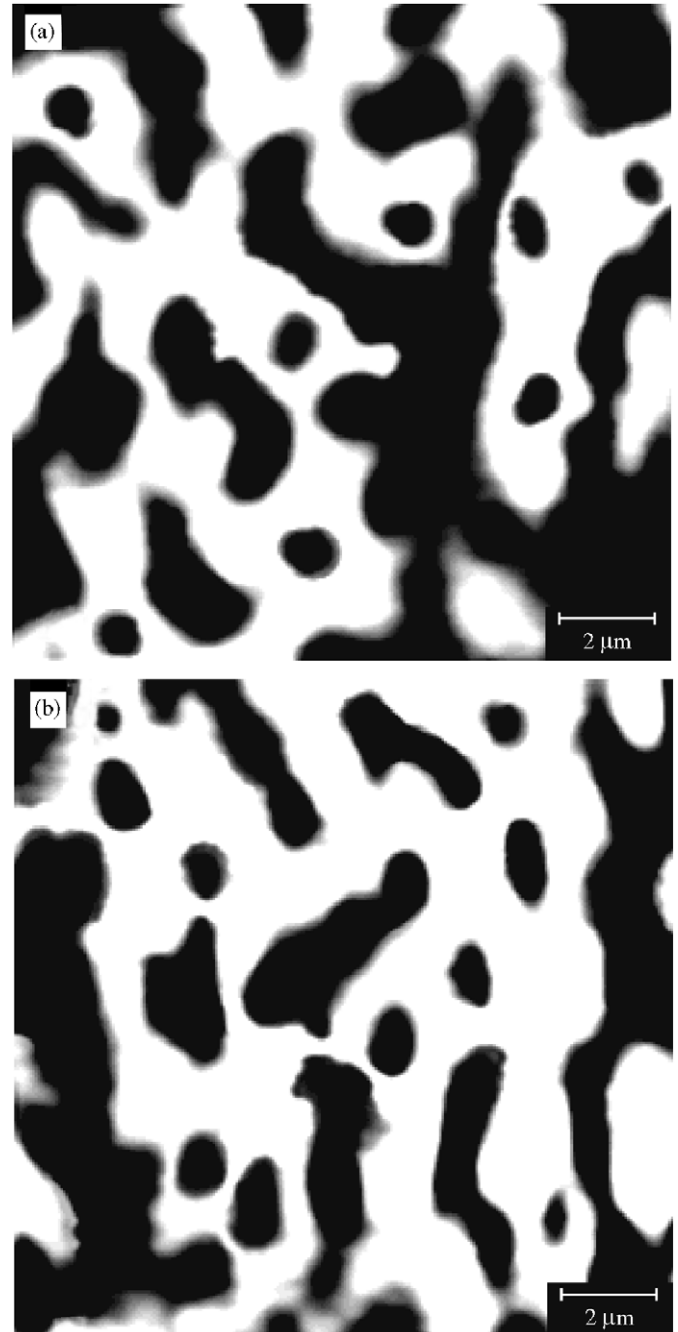

Fig. 2. Domain structure of specimens B (a) and D (b) in the thermally demagnetized state on the surface perpendicular to the alignment axis, revealed by the colloid-SEM method.

technique offers a spatial resolution of the order of 0.1 μm [38], which is not in fact limited by the resolution of the SEM but mainly by the quality of the colloids and of the specimen surface [38,39].

The domain structure was also studied by MFM, which offers high spatial resolution (routinely better than 100 nm), high surface sensitivity and ease of application. For these reasons the MFM method appears to be currently the most widely used. However, it is worth noting here that in close proximity to the surface

perpendicular to the alignment axis, Nd–Fe–B-based magnets exhibit a large magnetic induction, of the order of 10 kG. On the one hand, this may be seen as an unfavorable circumstance for MFM observations due to the expected perturbation of the magnetic state of the tip, but on the other hand, this leads to large interaction forces or force gradients and high contrast images, being a favorable condition. Typical MFM images of the domain structure are shown in Fig. 3, for specimens A (Fig. 3a) and C (Fig. 3b). The presence of maze domains and reverse
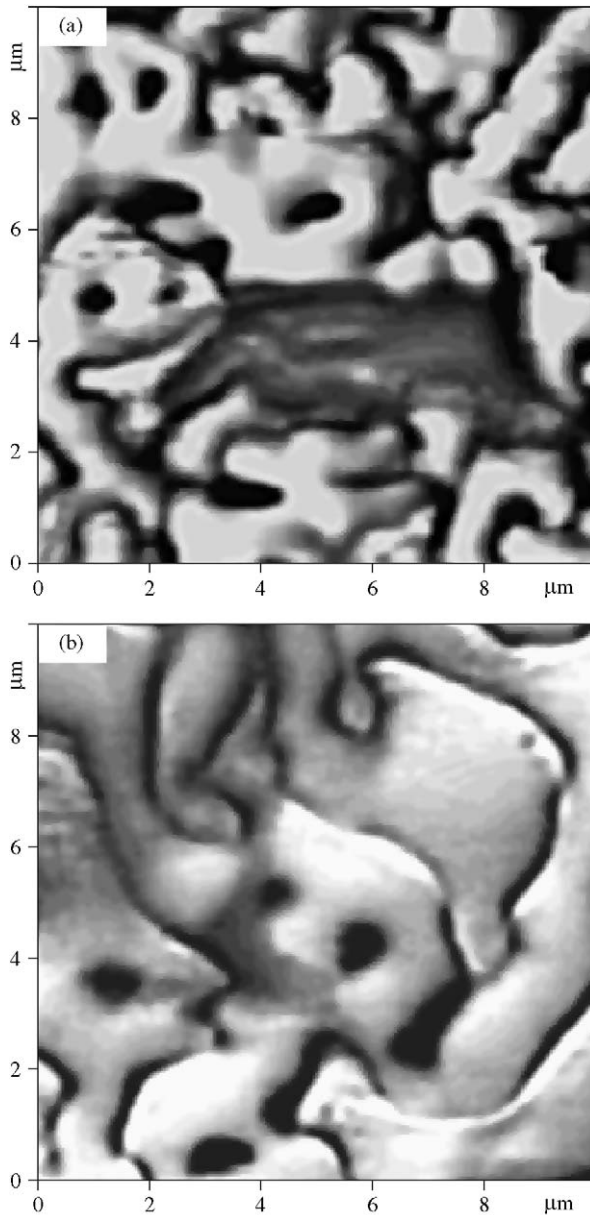
Fig. 3. MFM images of specimens A (a) and C (b) in the thermally demagnetized state on the surface perpendicular to the alignment axis, recorded with a tip–specimen distance of 100 nm.

spikes in these images is apparent. The domain walls are displayed as dark, while the main (maze) domains are substantially imaged as bright. The latter means that during scanning process the tip was remagnetized by the stray fields of main domains each time when passing from one domain to a neighboring domain (i.e. at the domain walls), resulting in the loss of information on their sign. This is as expected because near the surface their stray fields are much larger than the coercivity of the tip. In general, however, there were exceptions to this, although very rare. One such exception is the region near the central part of the image in Fig. 3a, where the neighboring main domains are visible as dark and bright and the boundaries between them are not clearly marked (see also Ref. [40]).

On the other hand, because the reverse spikes are relatively small, conically shaped, surface domains which contain only a small amount of material, their stray fields are insufficient to remagnetize the tip and they are substantially imaged as dark, indicating that their magnetization is opposite to that of the main domains within which they are located. In the context of interpreting MFM images of hard magnetic materials, it should be noted that depending on the degree of perturbation of the magnetic state of the tip by the specimen stray field, image contrast can arise between neighboring domains, or at domain walls, or can be a combination of both, as demonstrated in Ref. [20].

However, a detailed examination of the magnetic structure by the MFM technique shows that in addition to the coarse main domains and reverse spikes, a complicated system of fine scale surface domains in the shape of curved stripes is present. This fine domain structure was observed on all the specimens A–D studied, on various places of the surface. Examples are presented in high-resolution images of Fig. 4a (for specimen C) and Fig. 5a (for specimen D), while Figs. 4b and 5b show the corresponding AFM topographic data, respectively. No correlation was found between a given MFM image with the fine scale domain structure and the corresponding surface topography image, and moreover no change of the MFM image with changing scan direction was observed. This in turn means that the fine structure is of magnetic origin, and not an image artifact. In this context, it should be noted that the existence of the fine domain structure was reported for the first time for a monocrystalline $Nd_2Fe_{14}B$ specimen in Refs. [19,41], and then for Nd–Fe–B-based magnet (specimen B) in Ref. [42]. The fine scale domain structure of specimens A–D was in fact inhomogeneous, i.e. it varied in size and shape when we moved from one area of the surface to another. In this respect, it was similar to that present in anisotropic sintered $SmCo_5$ magnets (reported for the first time in Ref. [43]), and in contrast to the regular fine pattern observed in a monocrystalline $Nd_2Fe_{14}B$ specimen [19,41]. In general, the width of the fine domains in specimens A–D was in a wide range 20–250 nm.

The MFM method detects the stray field of the specimen and consequently is insensitive to in-plane component of magnetization. (In the case of specimens with in-plane magnetization, the only sources of the stray field are the domain walls and surface defects [30,31].) However, for the studied Nd–Fe–B-based magnets, the hard magnetic phase (from which these magnets are mainly composed) has a large magnetocrystalline anisotropy along the alignment axis, resulting in the large Q-values ($Q > 4$; cf. Table 1). For this reason, it is unlikely that the fine scale domains had a component of magnetization parallel to the specimen surface. Thus, the fine scale domains are found to be magnetized perpendicular to the surface. Their presence is certainly related to the reduction of the magnetostatic energy close to the specimen surface. The fine domains, as opposed to the large main domains, are imaged at different gray shades. This means that the magnetostatic interaction
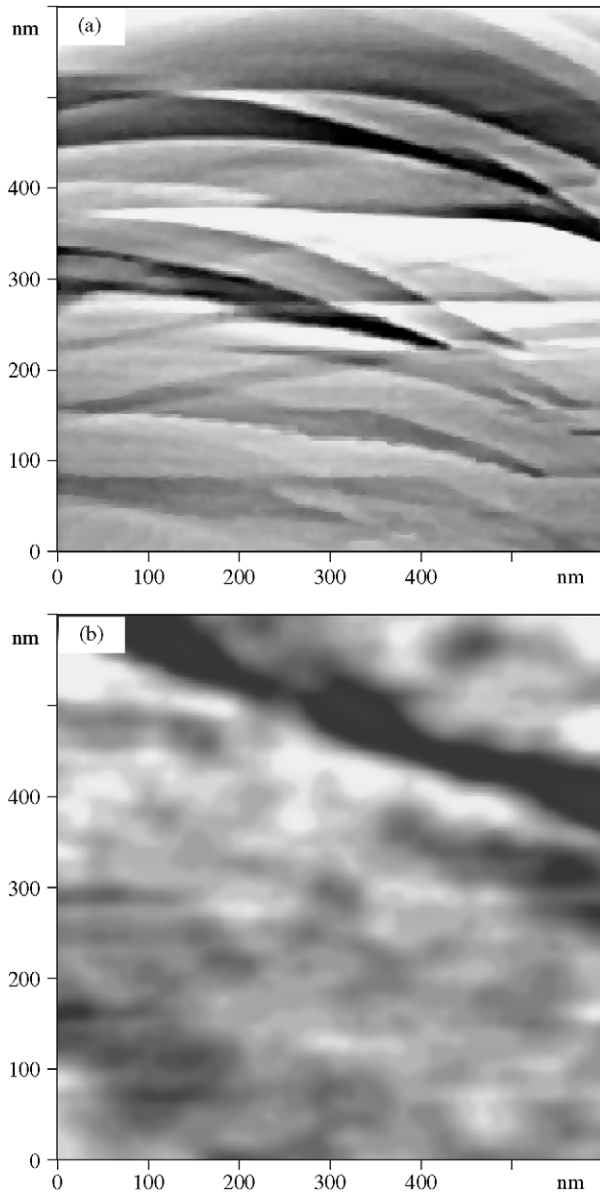
Fig. 4. High-resolution MFM image of specimen C in the thermally demagnetized state on the surface perpendicular to the alignment axis, taken with a tip–specimen distance of 100 nm (a), and the corresponding AFM image (b).
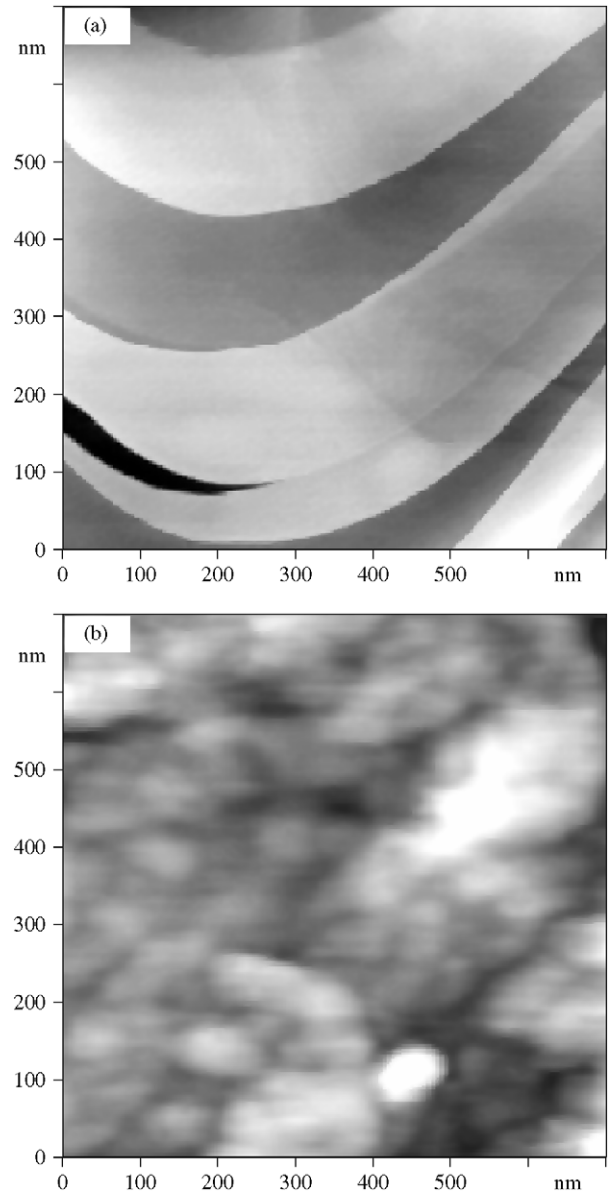
Fig. 5. High-resolution MFM image of specimen D in the thermally demagnetized state on the surface perpendicular to the alignment axis, recorded with a tip–specimen distance of 100 nm (a), and the corresponding AFM image (b).

between them and the tip was non-perturbing. However, because the fine scale domains are all magnetized perpendicular to the surface, this also means that they are located at different depths below the specimen surface, being a consequence of the fact that the domains lying deeper into the specimen produce weaker stray fields and thus different MFM signals than those located closer to the surface (accordingly, they are found not to cross). The described effect is seen in the images of Figs. 4a and 5a. The fine domains are found to lie close to the specimen surface, generally not deeper than about 100 nm (being of the order of their maximum width and of the distance over which their stray fields extend above the surface), because otherwise they could not be imaged so sharply as evidenced

in the MFM images. Moreover, these domains are generally expected to extend over a small depth into the specimen because otherwise a decrease in the magnetostatic energy would be smaller than the corresponding expense in the domain wall energy [43].

It is to be noted that the fine scale domains were not seen in images taken with the colloid-SEM technique. Nevertheless, this is in accordance with expectations, due to insufficient spatial resolution of the mentioned method. In fact, using this method, we were able to resolve magnetic domains of 0.3 μm in size [44], the result being very close only to the upper limit (250 nm) of the width range of the fine domains observed by MFM. In Ref. [38], it is stated that the spatial resolution of the colloid-SEM method is

approximately 0.1 μm, but it must be remembered, as already mentioned, that the spatial resolution of this method is not limited by the resolution of the SEM but mainly by the quality of the colloids and of the specimen surface [38,39].

Although with some difficulty, we have also succeeded in observing the domain structure of the studied Nd–Fe–B-based magnets by the type-I magnetic contrast method in the SEM. Examples of domain images are shown in Fig. 6, for specimens A (Fig. 6a) and C (Fig. 6b). Such observations were reported for the first time in Ref. [45] and

are in fact difficult because the magnetic signal is weak and additionally superimposed on a large amount of topographic contrast. In the images of Fig. 6, the contrast due to the magnetic domain structure corresponds to alternate dark gray and light gray stripes, while more sharply delineated objects displayed in black and white are due to the surface topography. Because of insufficient spatial resolution of the method (of about 1 μm), only the main domains could be observed. For obvious reasons, it is also difficult to determine the domain width from type-I magnetic contrast images. Nevertheless, comparison of the images presented in Fig. 6 shows that the main domains in specimens C were noticeably larger than those in specimens A.

Investigations carried out by the conventional Bitter pattern technique, the colloid-SEM method and MFM showed the presence of the domain pattern in the form of the maze (main) structure and reverse spikes practically on the whole specimen surface, indicating good magnetic alignment of the individual grains. Some misaligned grains were observed, but they were very rare. An example of such misaligned grain is presented in the image of Fig. 7, recorded with the conventional Bitter pattern technique. In the central part of the grain, the domain structure consists, to a good approximation, of stripe domains with parallel straight domain walls.

The observed maze domain structure with reverse spikes is characteristic of the surface perpendicular to the easy magnetization axis for sufficiently thick uniaxial materials with high magnetic anisotropy, as for example magneto-plumbite ($PbFe_{12}O_{19}$), barium ferrite ($BaFe_{12}O_{19}$) or samarium-cobalt ($SmCo_5$), for which $Q > 1$. The cause for the undulation of the main domains (the maze structure)
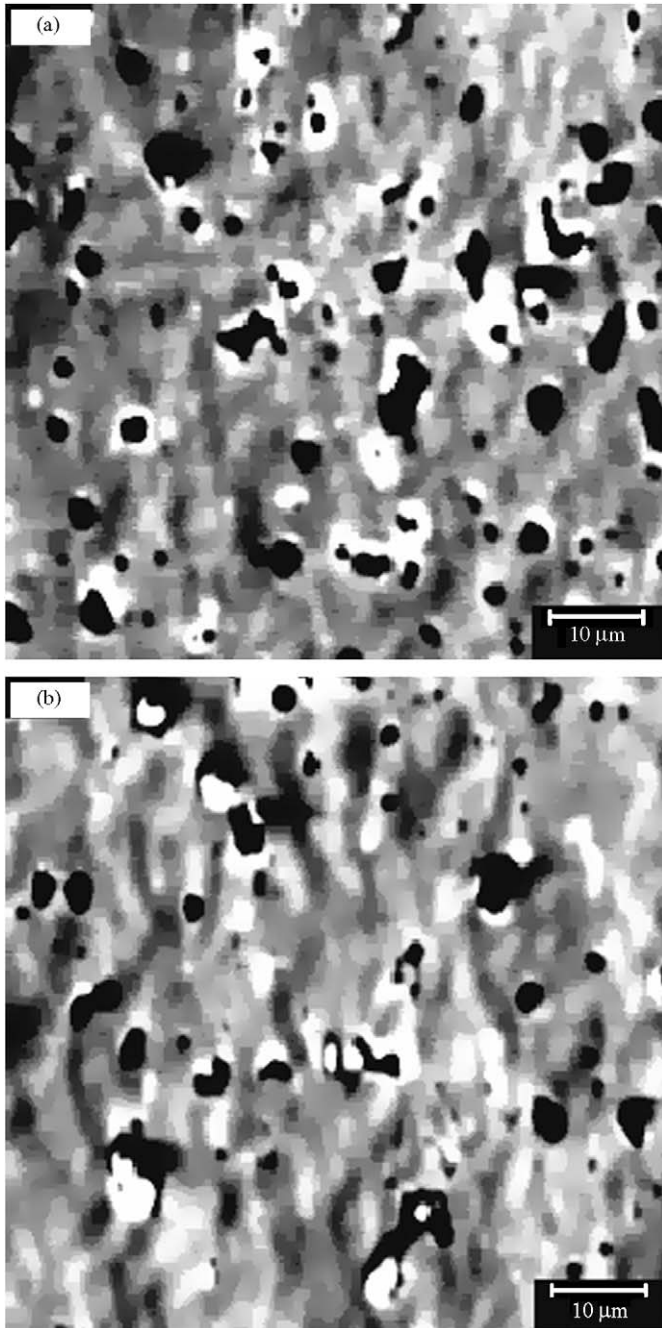

Fig. 6. Domain structure of specimens A (a) and C (b) in the thermally demagnetized state on the surface perpendicular to the alignment axis, made visible with the SEM type-I magnetic contrast.
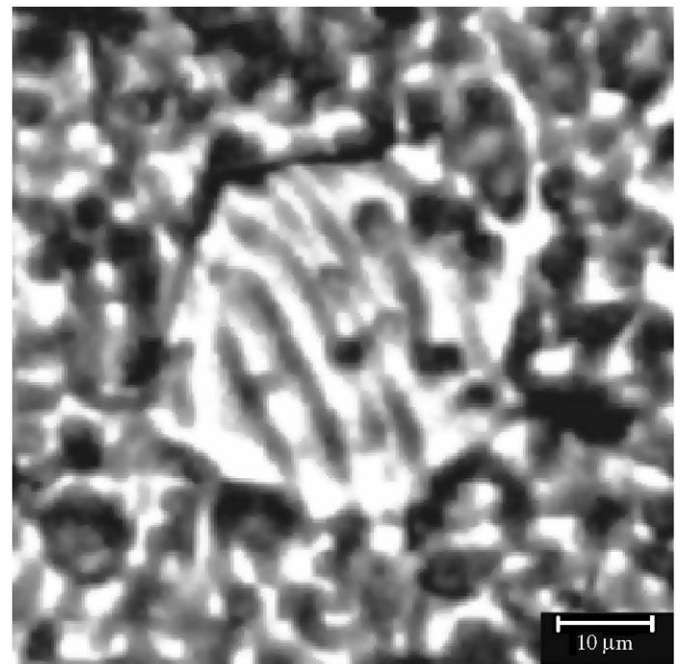

Fig. 7. Image of misaligned grain in specimen B in the thermally demagnetized state on the surface perpendicular to the alignment axis, obtained by the conventional Bitter pattern method.

and the occurrence of reverse spike domains (i.e. branching of the main domains) near the surface is the reduction in the magnetostatic energy at the cost of a larger total Bloch wall area [46].

3.2. Study of the domain structure in the thermally demagnetized state on the surface parallel to the alignment axis

Typical images of the magnetic structure in the thermally demagnetized state on the surface parallel to the alignment axis (axial plane), obtained by the colloid-SEM method and the conventional Bitter pattern technique, are shown in Figs. 8 and 10a, respectively. Practically, each $Nd_2Fe_{14}B$ grain has a multidomain structure. This is to be expected because the average grain size of about 10 μm exceeds considerably the single-domain particle diameter (cf. Table 6). The strong magnetocrystalline anisotropy of the tetragonal $Nd_2Fe_{14}B$ matrix phase, which is necessary for achieving a high coercivity, causes that the magnetic alignment is preferentially along the c-axis. From this, information on the alignment of the c-axis of individual grains can be obtained in a straightforward way. In all the specimens studied, magnetic alignment of the grains was found to be good, with the domain walls lying nearly parallel to the alignment axis across almost the whole specimen surface. In some cases, visible also in the presented images, the domain walls were observed to continue through the grain boundaries, suggesting that neighboring grains are magnetically coupled. Nevertheless, usually the domain patterns within individual grains were different in the sense that the domain structure of a given grain was not influenced by magnetization distributions of its neighbors. This in turn means exchange decoupling of the grains from each other, due to the presence of non-magnetic phases between the grains, and consequently allows one to obtain a high coercivity [25,47]. Otherwise, magnetization reversal of one grain could trigger the magnetization reversal of neighboring grains, resulting in a decrease of the coercivity. The images also show that reverse spike domains are present near some grain boundaries, pores and precipitations. The existence of misaligned grains was observed, but they were very rare. Deviations in the domain structure from that of the correct axial plane are due to an imperfect alignment of the c-axis of the grains. In this context, it is worth noting that an improved alignment of the hard magnetic grains results in higher energy density on the one hand, but on the other hand it leads to a decrease of the coercivity of magnets [48].

3.3. Determination of the surface and main domain widths

It is easy to define the domain width for simple domain configurations and in such cases it can be determined to a good or very good accuracy by visual method. However, in the case of complicated domain patterns, as those of the studied Nd–Fe–B-based magnets in the thermally demag-
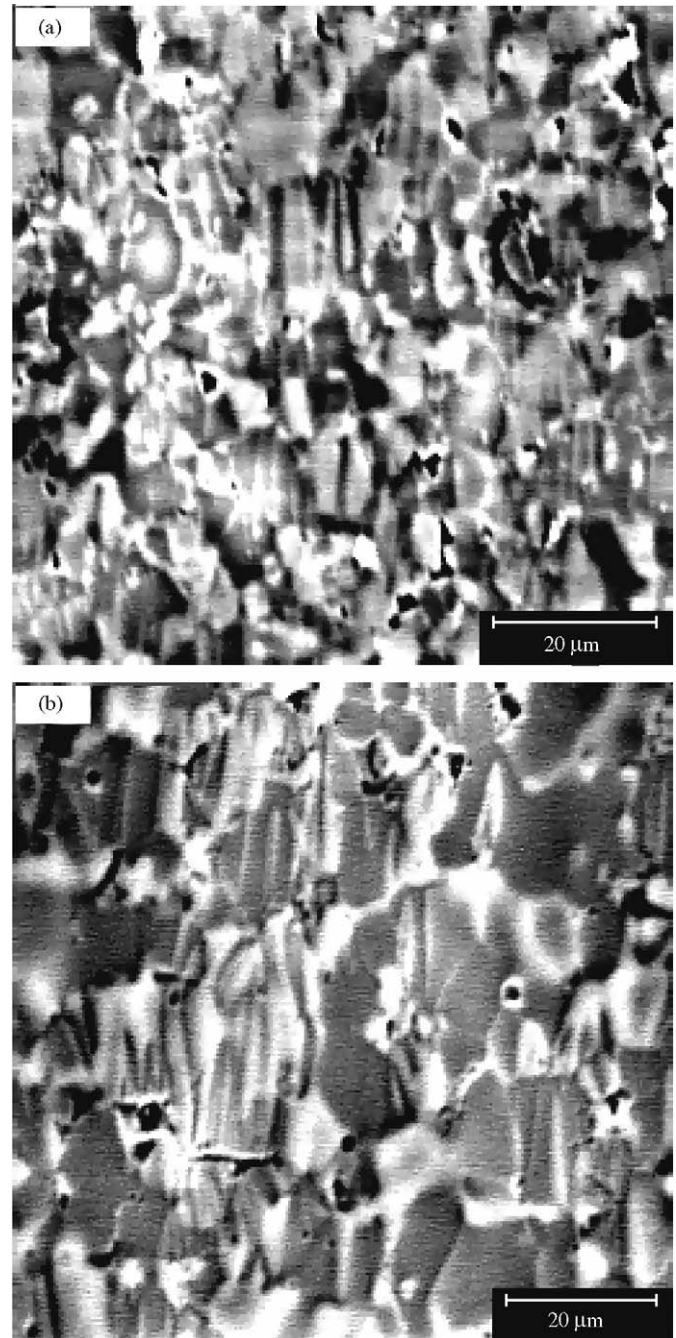

Fig. 8. Images of the domain structure of specimens A (a) and D (b) in the thermally demagnetized state on the surface parallel to the alignment axis, taken with the colloid-SEM technique.

netized state on the surface perpendicular to the alignment axis, defining the domain width is not generally trivial and determining it with a digital method is found to be much more appropriate than by visual measurements. Therefore, we determined the domain width by digital means using the stereologic method proposed by Bodenberger and Hubert [49] (see also Ref. [50]), which appears to be the most universal and commonly applied method. In this method, an effective domain width is defined as the ratio of a chosen area to the total length of domain walls in this area. This
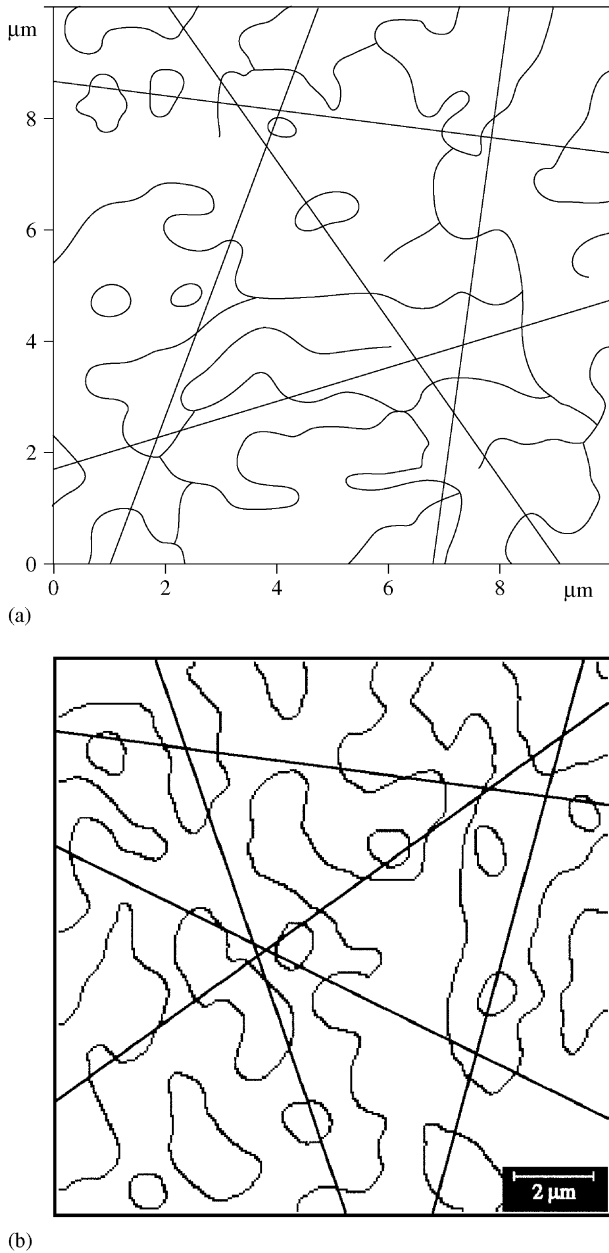
(a)

(b)

Fig. 9. Images (a) and (b) with the domain boundaries represented by black lines, corresponding to the MFM image of Fig. 3a and the colloid-SEM image of Fig. 2a, respectively. On these images, five test straight lines are additionally superimposed to illustrate the stereologic method of Bodenberger and Hubert used for determining the domain width.

definition of the domain width is in agreement with the ordinary definition for stripe domains with parallel straight walls. For the purpose of evaluating the total domain wall length, a large number of test straight lines running in random directions is used; the method is illustrated in the images of Fig. 9, where five test lines are drawn on each image. The domain width D is determined from the following formula:

$$D = (2/\pi)\left(\sum_i l_i\right)\Big/\left(\sum_i n_i\right),\tag{1}$$

where l_i is the length of the ith test line and n_i is the number of intersections of the ith test line with domain walls.

One must be aware that determination of the domain width requires application of domain observation method with sufficiently high spatial resolution. In the case of the studied Nd–Fe–B-based magnets, the results obtained by the conventional Bitter pattern technique and the SEM type-I magnetic contrast clearly show that these methods are not suitable for this purpose (see Section 3.1). As a consequence, the domain width was determined on the basis of images recorded by the colloid-SEM technique and MFM.

In the case of images obtained with the colloid-SEM method, the image contrast is observed between the domains (cf. Fig. 2). To determine the positions of domain walls in the image, the digital procedure presented in Ref. [34] was applied. First, a gray-scale image with the domain structure was transformed to the corresponding black-and-white image by a simple thresholding technique on the level of the average image intensity, and then a 3×3 pixel median filter was applied for the purpose of smoothing the latter image and removing from it some possible artifacts in the form of small objects produced by the thresholding technique. This resulted in the image, from which using a simple digital procedure it was easy to derive the corresponding image, where the domain boundaries are represented by black lines.

In the considered context, the situation is more complicated for $10\,\mu m \times 10\,\mu m$ images (cf. Fig. 3) taken by the MFM technique. Here the image contrast is observed between the main (maze) domains and reverse spikes, while the main domains are substantially imaged as bright (i.e. the domain walls separating the main domains are in contrast). Moreover, there were exceptions to this (in fact very rare), the domain boundaries between the main domains are imaged as comparatively wide (the domain walls in Nd–Fe–B-based magnets are very narrow, only about 6–8 nm in thickness, as given in Table 6), and what is found to be much more undesirable, within the main domains and the domain walls separating them there are generally quite large variations in the intensities of the image points. All these features cause that deriving the positions of domain walls in the MFM image by a digital procedure similar to that applied to the colloid-SEM image was impossible; as a consequence, they had to be determined manually.

Fig. 9a and b shows the resultant images with the domain boundaries represented by black lines, corresponding to the MFM image of Fig. 3a and the colloid-SEM image of Fig. 2a, respectively. On the basis of such images, the surface domain width D_s was determined by applying the stereologic method with 1000 test straight lines (on the images of Fig. 9, five test straight lines are additionally superimposed); to evaluate the accuracy of determining the domain width, the procedure was repeated 10 times. Then the surface domains (reverse spikes) were removed (manually) from the considered images, and to determine

Table 2
Experimental values of the main domain width D_m and the surface domain width D_s for the studied Nd–Fe–B-based magnets

Specimen	D_m (µm)	D_s (µm)
A	1.16 ± 0.06	0.89 ± 0.06
B	1.34 ± 0.07	1.13 ± 0.07
C	1.59 ± 0.06	1.45 ± 0.06
D	1.25 ± 0.07	1.03 ± 0.06

the main domain width D_m, the stereologic method was applied again. The results obtained for the studied Nd–Fe–B-based magnets are presented in Table 2. The given domain widths represent averages from 10 images (five images were recorded by the colloid-SEM technique and five images were collected with MFM) of the domain structure taken at various places on the specimen surface.

3.4. Determination of the domain wall energy

The domain wall energy, being to a very good approximation the sum of contributions from the exchange and magnetic anisotropy energies, is a fundamental parameter related to the coercivity issue. The knowledge of this parameter is of great significance irrespective of the fact whether nucleation of reverse domains or pinning of domain walls is the dominant mechanism of magnetic hardening. The domain wall energy can be obtained on the basis of investigations of the magnetic domain structure.

The domain structure of sufficiently thin uniaxial crystals with high magnetic anisotropy can be very well described by the Kittel's [51] parallel-plate domain configuration, for which the dependence of the domain width D on the crystal thickness L, taking into account the μ^*-correction introduced by Kooy and Enz [52], is given by

$$D = [\gamma(1 + \mu^{*1/2})/3.4 M_s^2]^{1/2} L^{1/2}, \qquad (2)$$

where γ is the domain wall energy and $\mu^* = 1 + Q^{-1}$ is the rotational permeability of the material (the μ^*-effect is related to deviation of the magnetization from the magnetic easy axis due to the stray field).

As the crystal thickness increases, the domain structure becomes more complicated. It first shows, above a critical thickness L_{cr1}, an undulation of the Bloch walls near the surface perpendicular to the easy magnetization axis, and then, above a critical thickness L_{cr2}, the formation of surface reverse spikes. As previously mentioned, the reason for this is the reduction in the magnetostatic energy at the cost of a larger total Bloch wall area.

The wavy domain structure near the surface was considered for the first in the theoretical model of Goodenough [46], which was subsequently generalized by the model of Szymczak [53,54]. The latter model gives the following relationships concerning the critical crystal thickness:

$$L_{cr1} = 26.39\gamma/\mu^{*2} M_s^2 \qquad (3)$$

and the dependence of the domain width D on the crystal thickness L for the wavy domain structure:

$$D = 0.54\gamma^{0.4}\mu^{*0.2} M_s^{-0.8} L^{0.6}. \qquad (4)$$

Above the critical crystal thickness L_{cr2}, the presence of surface reverse spikes (i.e. branching of the main domains) takes place. In this case, the dependence of the width of the main domains D_m on the crystal thickness L is a power dependence with an exponent close to 2/3, as proved experimentally for a number of uniaxial ferromagnets. The dependence $D_m \sim L^{2/3}$ was derived theoretically for the first time in the model of Kaczér [55], and it is also predicted by the model of Hubert [50,56] and the extended model of Szymczak [9,57]. Because of the simplifications assumed in these models, they are not certainly very good representations of the real, much more complex domain structure. Nevertheless, the mentioned models appear to be the most frequently used for description of the domain structure of uniaxial materials for crystal thicknesses larger than L_{cr2}.

The critical thickness L_{cr2} is predicted by the model of Kaczér [55] as

$$L_{cr2} = 16\pi^2\gamma/1.7^3\mu^{*2} M_s^2 \qquad (5)$$

and by the model of Hubert [50] as

$$L_{cr2} = 24.07\gamma(1 + \mu^{*1/2})^3/\mu^{*2} M_s^2. \qquad (6)$$

The dependence D_m versus L is given in the model of Kaczér [55] by the formula

$$D_m = (3/8M_s)^{2/3}(\gamma\mu^*/\pi)^{1/3} L^{2/3}, \qquad (7)$$

in the model of Hubert [50] by the formula

$$D_m = (4\gamma\mu^*/\pi^3 M_s^2)^{1/3} L^{2/3}, \qquad (8)$$

and in the extended model of Szymczak [9,57] by the formula

$$D_m = 0.395(\gamma\mu^*/M_s^2)^{1/3} L^{2/3}. \qquad (9)$$

The most reliable way of determining the domain wall energy appears to be based on Eq. (2), which is related to the Kittel's parallel-plate domain configuration. This is because the validity of formula (2) is very well established, the domain structure is in this case fairly simple and the domain width can be determined experimentally with a high accuracy. To derive the domain wall energy from Eq. (2), we need to know the crystal thickness L, the domain width D, the magnetic anisotropy constant K and the saturation magnetization M_s ($\mu^* = 1 + 2\pi M_s^2/K$).

In Table 3, we present the values of the domain wall energy γ obtained using Eq. (2) for various uniaxial materials with high magnetic anisotropy (for which $Q > 1$), taken from the literature. Table 3 shows also comparison of the experimentally determined critical crystal thicknesses L_{cr1} with those predicted by the theoretical model of Szymczak, and the experimentally determined critical crystal thicknesses L_{cr2} with those predicted by the theoretical models of Kaczér and Hubert. It should be noted that, unsatisfactorily, there are

Table 3
Data for various uniaxial materials with high magnetic anisotropy (for which $Q>1$), taken from the literature

Crystal	M_s (G)	K (erg/cm³)	Q	$\gamma^{(KE)}$ (erg/cm²) [Ref.]	$L_{cr1}^{(exp)}$ (μm) [Ref.]	$L_{cr1}^{(S)}$ (μm)	$L_{cr2}^{(exp)}$ (μm) [Ref.]	$L_{cr2}^{(K)}$ (μm)	$L_{cr2}^{(H)}$ (μm)
BaFe$_{12}$O$_{19}$	370	3.3×10^6	3.8	2.6 [52]	10 [58,59,53]	3.4	50 [58,53]	4.1	29.6
BaFe$_{12}$O$_{19}$	380	3.4×10^6	3.7	6.6 [58]	10 [58,59,53]	8.0	50 [58,53]	9.7	69.8
BaFe$_{12}$O$_{19}$	380	3.4×10^6	3.7	8.5 [59]	10 [58,59,53]	10.2	50 [58,53]	12.5	89.8
PbFe$_{12}$O$_{19}$	320	2.2×10^6	3.4	4.7 [60]	10 [61,53]	7.7	50 [61,53]	9.4	68.7
PbFe$_{12}$O$_{19}$	320	2.2×10^6	3.4	4.5 [61]	10 [61,53]	7.4	50 [61,53]	9.0	65.9
SrFe$_{12}$O$_{19}$	350	3.7×10^6	4.8	7.6 [59]	10 [59]	11.8	≈50 [62]	14.4	99.6
SrFe$_{12}$O$_{19}$	380	3.7×10^6	4.1	3.6 [62]	10 [59]	4.5	≈50 [62]	5.5	39.1
YCo$_5$	848	5.0×10^7	11.1	34.2 [63]	10 [63,64]	10.8	30 [63]; 50 [64]	13.2	84.2
YCo$_5$	848	5.0×10^7	11.1	33.3 [64]	10 [63,64]	10.5	30 [63]; 50 [64]	12.8	81.8
SmCo$_5$	855	1.3×10^8	28.3	84.3 [63]	≈10 [63]	28.6	≈20 [63]; ≈10 [49]	34.9	214.4
SmCo$_5$	880	1.3×10^8	26.7	73.3 [49]	≈10 [63]	23.4	≈20 [63]; ≈10 [49]	28.5	175.8
CeCo$_5$	615	3.0×10^7	12.6	24.5 [63]	≈10 [63]	15.0	≈30 [63]	18.2	115.8
PrCo$_5$	960	9.0×10^7	15.5	39.4 [63]	<13 [63]	10.1	≈30 [63]	12.3	77.3

M_s is the saturation magnetization, K is the magnetocrystalline anisotropy constant, $Q = K/2\pi M_s^2$ is the relative magnetic anisotropy, $\gamma^{(KE)}$ is the domain wall energy determined using Eq. (2), $L_{cr1}^{(exp)}$ and $L_{cr1}^{(S)}$ are the critical thickness above which an undulation of the Bloch walls (near the surface perpendicular to the easy magnetization axis) takes place, determined experimentally and using Eq. (3) of the theoretical model of Szymczak [53,54], respectively, $L_{cr2}^{(exp)}$, $L_{cr2}^{(K)}$ and $L_{cr2}^{(H)}$ are the critical thickness above which surface reverse spikes are present, determined experimentally, using Eq. (5) of the theoretical model of Kaczér [55] and using Eq. (6) of the theoretical model of Hubert [50], respectively.

Table 4
Values of the domain wall energy for various uniaxial materials with high magnetic anisotropy (for which $Q>1$) obtained from the theory of Kaczér ($\gamma^{(K)}$), the theory of Hubert ($\gamma^{(H)}$) and the extended theory of Szymczak ($\gamma^{(eS)}$) for the cases taken from the literature, where domain studies for a particular material were carried out on a series of monocrystalline specimens of different thicknesses and the corresponding dependence of the main domain width D_m on the crystal thickness L was established for crystal thicknesses larger than the critical thickness above which surface reverse spikes are present

Crystal	M_s (G)	K (erg/cm³)	Q	$D_m = D_m(L)$ (cm) [Ref.]	$\gamma^{(K)}$ (erg/cm²)	$\gamma^{(H)}$ (erg/cm²)	$\gamma^{(eS)}$ (erg/cm²)
BaFe$_{12}$O$_{19}$	380	3.4×10^6	3.7	$0.0168L^{0.65}$ [58]	12.1	4.2	8.8
BaFe$_{12}$O$_{19}$	380	3.4×10^6	3.7	$0.0179L^{0.665}$ [59]	14.6	5.1	10.6
BaFe$_{12}$O$_{19}$	365	3.4×10^6	4.1	$0.0105L^{0.6}$ [53]	2.8	1.0	2.0
PbFe$_{12}$O$_{19}$	320	2.2×10^6	3.4	$0.0132L^{0.633}$ [61]	4.1	1.4	3.0
PbFe$_{12}$O$_{19}$	320	2.2×10^6	3.4	$0.0107L^{0.6}$ [53]	2.2	0.8	1.6
SrFe$_{12}$O$_{19}$	350	3.7×10^6	4.8	$0.0160L^{0.640}$ [59]	9.3	3.2	6.7
YCo$_5$	848	5.0×10^7	11.1	$0.0163L^{0.66}$ [64]	63.8	22.1	46.4

M_s is the saturation magnetization, K is the magnetocrystalline anisotropy constant, $Q = K/2\pi M_s^2$ is the relative magnetic anisotropy.

considerable differences between the experimental γ values determined in Refs. [52,58,59] for BaFe$_{12}$O$_{19}$, and also between those determined in Refs. [59,62] for SrFe$_{12}$O$_{19}$. Moreover, the agreement between the theoretical L_{cr1} values obtained in the model of Szymczak and the experiment is found to be good, much better than that between the theoretical L_{cr2} values obtained in the models of Kaczér and Hubert and the experiment.

For all the Nd–Fe–B-based magnets studied by us in this paper, which were composed of grains with an average size of about 10 μm, the wavy domain structure with reverse spike domains was present. Such a domain structure was also observed in Refs. [5,9,11,19,41] for monocrystalline Nd$_2$Fe$_{14}$B specimens with thicknesses larger than about 10 μm. In Ref. [18], the domain wall energy of sintered Nd–Fe–B-based compounds was determined by TEM using specimens with thicknesses in the range 40–100 nm (which exhibited stripe domains) and employing an energy minimization model. Nevertheless, as far as the author is aware, the domain wall energy of Nd–Fe–B-based compound has not yet been determined using sufficiently thin crystals (thinner than 10 μm), where the Kittel's parallel-plate domain structure occurs (to a very good approximation) and Eq. (2) can be applied.

The domain wall energies of the Nd–Fe–B-based magnets investigated by us in this work can be determined using the theory of Kaczér, the theory of Hubert and the extended theory of Szymczak, i.e. on the basis of Eqs. (7)–(9), respectively. For the purpose of comparison of the mentioned theories, we give in Table 4 the γ values for various uniaxial materials with high magnetic anisotropy (for which $Q>1$) obtained from these theories for the cases taken from the literature, where domain studies for a particular material were carried out on a series of monocrystalline specimens of different thicknesses and the corresponding dependence of the main domain width D_m on the crystal thickness L was established for crystal thicknesses larger than the critical thickness L_{cr2}. Firstly, it

should be noted that, unsatisfactorily, within each of the considered theoretical models there are considerable differences between the γ values obtained for $BaFe_{12}O_{19}$, and also for $PbFe_{12}O_{19}$. Secondly, as the γ values presented in Table 4 are compared with those collected in Table 3 (taking the average values for $BaFe_{12}O_{19}$, $PbFe_{12}O_{19}$, $SrFe_{12}O_{19}$ and YCo_5), the conclusion is that the predictions of the extended theory of Szymczak are closest to the experiment, although of course we must be aware that the experimental data concerning γ (Table 3) and $D_m = D_m(L)$ (Table 4) obtained in different papers for the same material differ considerably and that the statistics for the comparison performed is in fact small.

The domain wall energies of the studied Nd–Fe–B-based magnets, resulting from the theory of Kaczér, the theory of Hubert and the extended theory of Szymczak, are presented in Table 5. Because of good agreement between the theoretical L_{cr1} values obtained in the model of Szymczak and the experiment and the fact that the predictions of the extended model of Szymczak concerning the γ values for various uniaxial materials with high magnetic anisotropy (for which $Q > 1$) are closest to the experiment, we are inclined to the statement that the results obtained with the use of the theory of Szymczak are the most reliable, however with bearing in mind the remarks given above.

Another way of obtaining the domain wall energy γ is to determine the surface domain width D_s for sufficiently large grains, which, according to the theory of Hubert [49,50], is predicted to have a constant value given as

$$D_s = 4\pi\beta\gamma/M_s^2, \tag{10}$$

where β is a coefficient dependent on the type of the surface domain structure. For uniaxial crystals with high magnetic

Table 5
Values of the domain wall energy for the studied Nd–Fe–B-based magnets determined using the theory of Kaczér ($\gamma^{(K)}$), the theory of Hubert ($\gamma^{(H)}$) and the extended theory of Szymczak ($\gamma^{(eS)}$)

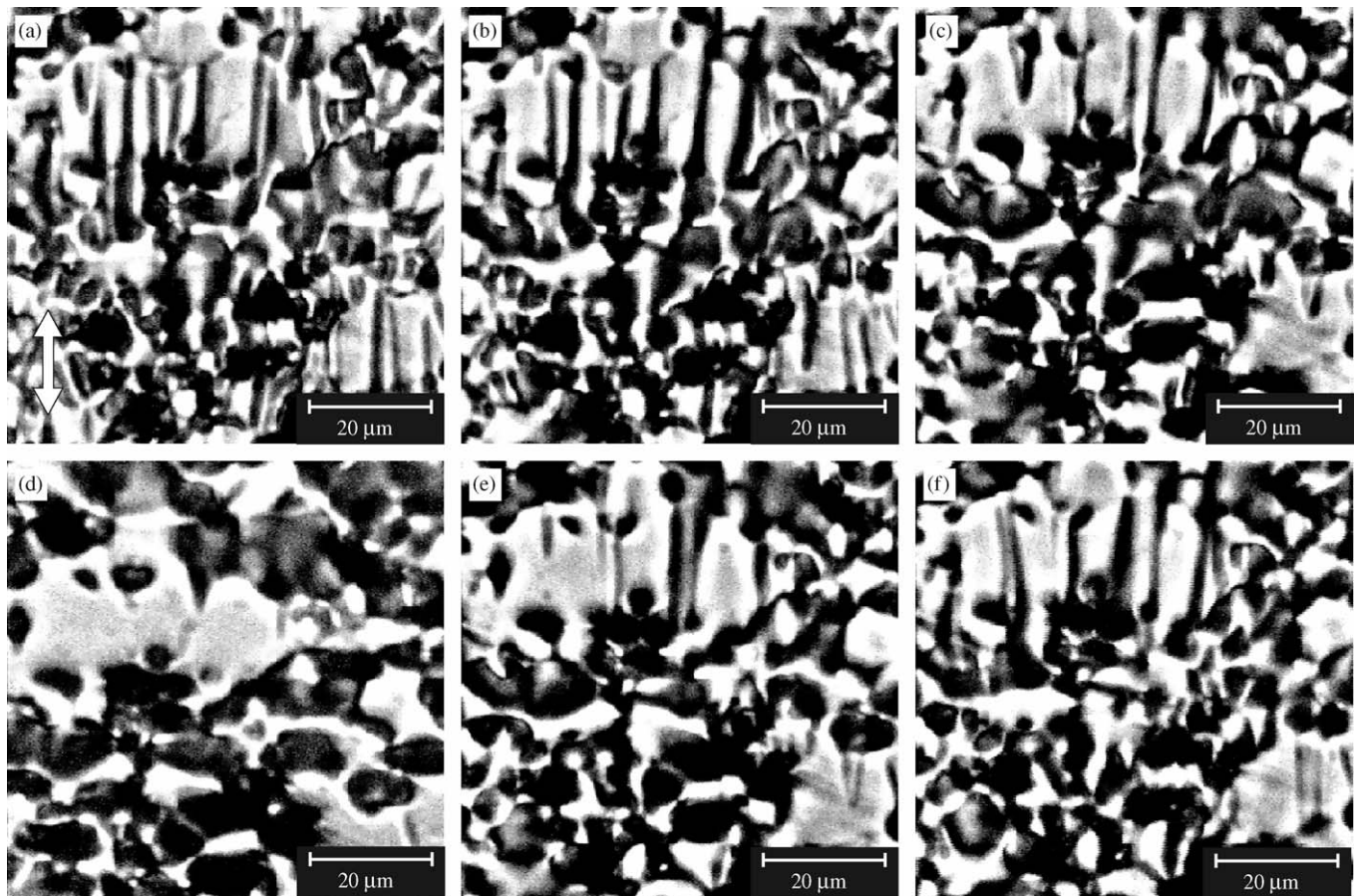| Specimen	$\gamma^{(K)}$ (erg/cm^2)	$\gamma^{(H)}$ (erg/cm^2)	$\gamma^{(eS)}$ (erg/cm^2)
A	37 ± 6	13 ± 2	27 ± 4
B	47 ± 7	16 ± 3	34 ± 5
C	67 ± 8	23 ± 3	48 ± 6
D	51 ± 8	18 ± 3	37 ± 6

Fig. 10. Effect of magnetizing cycle on the magnetic structure of specimen D on the surface parallel to the alignment axis, imaged by the conventional Bitter pattern technique. The external magnetic field was parallel to the alignment axis, indicated by double headed arrows in (a) and (g). 0 Oe (a) → 600 Oe (b) → 2 kOe (c) → 4.8 kOe (d) → 2 kOe (e) → 800 Oe (f) → 0 Oe (g) → −600 Oe (h) → −2.6 kOe (i) → −4.8 kOe (j) → −1.1 kOe (k) → 0 Oe (l).
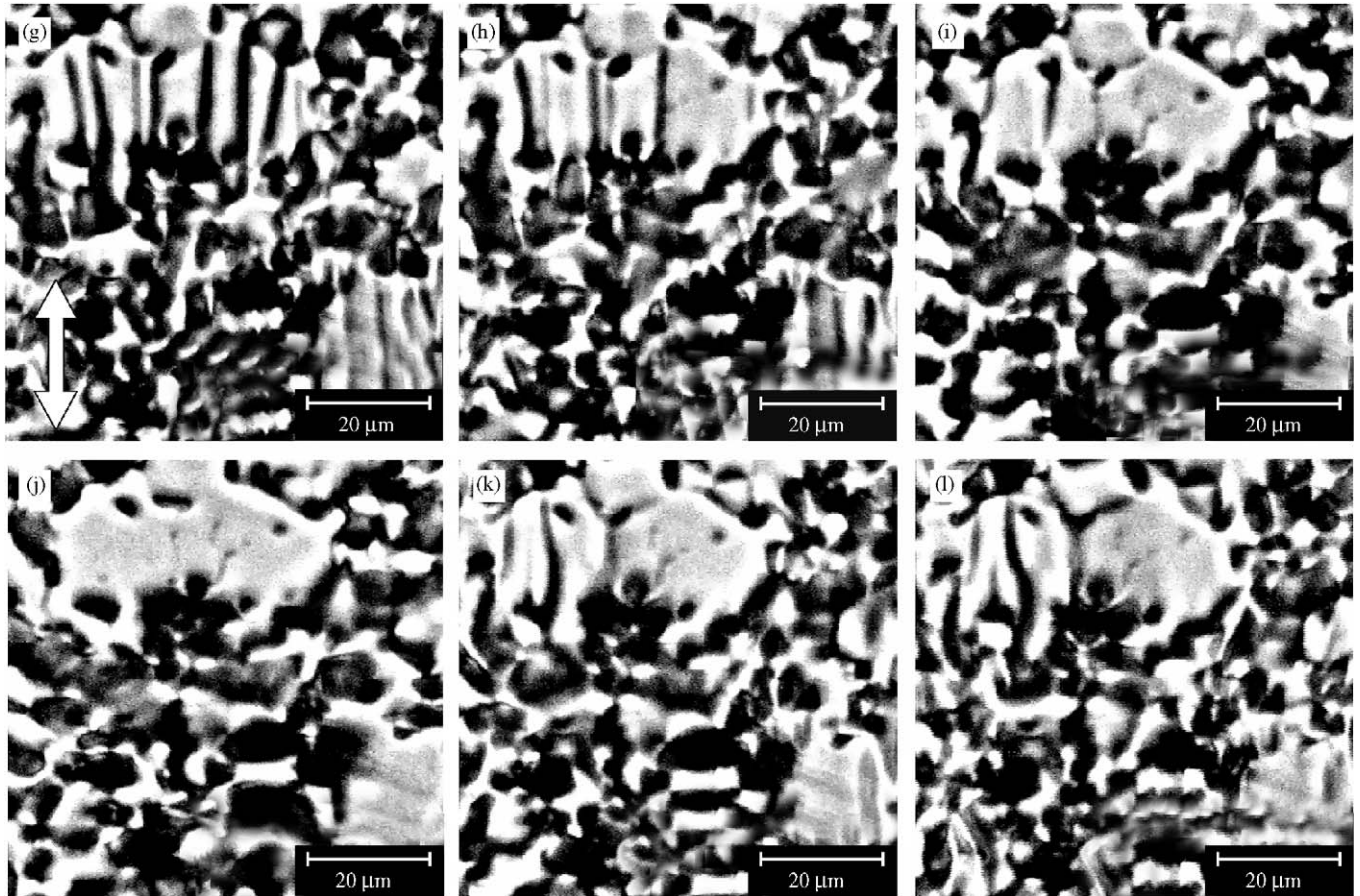
Fig. 10. (*Continued*)

anisotropy (for which $Q > 1$), the coefficient β is usually assumed to be 0.31, although in reality it was determined only for $SmCo_5$ [49] and YCo_5 [64]. In Refs. [9] and [11], it was found that for $Nd_2Fe_{14}B$ the surface domain width becomes constant for crystal thickness larger than about 100 and 80 μm, respectively. Nevertheless, in the case of the Nd–Fe–B-based magnets investigated by us in this work, the existence of grains of such large size was not observed.

As previously mentioned, observations carried out on the axial surfaces of the Nd–Fe–B-based magnets in the thermally demagnetized state, using the colloid-SEM method and the conventional Bitter pattern technique, showed that in most cases the main domains within individual grains were stripe domains with domain walls running nearly parallel to the alignment axis. Nevertheless, usually the distances between neighboring domain walls were not the same but differed to a considerable degree, and in some cases the positions of domain walls were invisible or only slightly marked (cf. Figs. 8 and 10a). (It is to be noted that the latter effect was also reported in Refs. [5,6] for the case of domain observations by magneto-optic Kerr microscopy.) Moreover, the grains are generally irregular in shape, which makes determination of their thicknesses with a good accuracy practically impossible. For these reasons, determination of the dependence of the

main domain width D_m on the grain thickness L, and then derivation from this dependence the domain wall energy γ, were not found to be reliable.

3.5. Determination of the exchange constant, the domain wall thickness and the critical diameter for single-domain particle

The knowledge of the domain wall energy γ allows one to determine the exchange constant A, the domain wall thickness δ (using the standard continuum model of a domain wall) and the critical diameter for single-domain particle d_c, on the basis of the relationships given below:

$$\gamma = 4(AK)^{1/2}, \tag{11}$$

$$\delta = \pi(A/K)^{1/2} = \pi\gamma/4K, \tag{12}$$

$$d_c = 1.4\gamma/M_s^2. \tag{13}$$

The δ, d_c and A values for the investigated Nd–Fe–B-based magnets are collected in Table 6. They were obtained using the domain wall energies determined on the basis of the extended theory of Szymczak (see Section 3.4 and Table 5).

Table 6
Values of the domain wall thickness δ, the single-domain particle diameter d_c and the exchange constant A for the studied Nd–Fe–B-based magnets, obtained using the domain wall energies determined on the basis of the extended theory of Szymczak (cf. Table 5)

Specimen	δ (nm)	d_c (μm)	A (erg/cm)
A	5.7 ± 0.8	0.29 ± 0.06	$(1.2 \pm 0.5) \times 10^{-6}$
B	6.3 ± 0.9	0.48 ± 0.08	$(1.7 \pm 0.6) \times 10^{-6}$
C	8.1 ± 0.8	0.82 ± 0.09	$(3.1 \pm 0.7) \times 10^{-6}$
D	5.7 ± 0.9	0.38 ± 0.07	$(1.7 \pm 0.6) \times 10^{-6}$

3.6. Dependence of the domain structure on the Dy concentration

The effect of Dy addition on the domain structure of Nd–Fe–B magnets can be estimated on the basis of specimens A–C. All the considered specimens were obtained from NEOMAX Co., Ltd., and they were prepared, processed and sintered under same (or very similar) conditions. Additions of Dy greatly increase the magnetic anisotropy field H_a of Nd–Fe–B-based magnets (by partial substitution of Dy for Nd) [65–67], however at the cost of a smaller saturation magnetization M_s, resulting in an increased magnetic anisotropy constant K, an increased domain wall energy γ, an increased coercivity but a reduced energy product (cf. Tables 1 and 5). It is worth noting that in Ref. [65] it was found for $(Nd_{1-x}Dy_x)_{15}Fe_{77}B_8$ magnets that the magnetic anisotropy field and the saturation magnetization vary approximately linearly with the Dy concentration. The Dy substitution for Nd results also in modification of the domain structure. According to Eqs. (7)–(9), the main domain width is proportional to $(\gamma\mu^*/M_s^2)^{1/3}$. This means that an increase in the main domain width with increasing Dy concentration is expected, in agreement with the experimental results (cf. Tables 2 and 1).

The theoretical model of Hubert predicts the following relationship between the surface domain width D_s and the main domain width D_m [50]

$$D_s^{-1} - D_m^{-1} = 0.074\pi\mu^* M_s^2/\gamma(1 + \mu^{*1/2})^2. \qquad (14)$$

Using the above formula we obtain the surface domain widths 0.85, 1.08 and 1.36 μm for specimens A, B and C, respectively (the domain wall energies determined on the basis of the extended theory of Szymczak (see Section 3.4 and Table 5) were taken in the calculations). The theoretical values obtained agree well with the experiment (cf. Tables 2 and 1).

3.7. Study of the domain structure in an external magnetic field

The conventional Bitter pattern technique has the advantage that it allows one to observe the evolution of domain configuration under the influence of an applied magnetic field. In this way, useful information about magnetizing and demagnetizing processes can be obtained. A typical behavior of the domain structure of the studied Nd–Fe–B-based magnets, on the surface parallel to the alignment axis, through a complete cycle is presented in Fig. 10, where the external magnetic field was applied along the alignment axis.

In the demagnetized state (Fig. 10a), practically each $Nd_2Fe_{14}B$ grain consists of domains, as expected. As the external magnetic field was increased (Fig. 10b–d), easy domain wall displacements within the grains were observed at low fields of a few hundred oersteds, leading to growth of the domains with magnetization oriented in the direction of the field and the corresponding decrease of those with opposite magnetization. This indicates that no significant domain wall pinning took place within the grains. As a result, steep initial magnetization curves and large susceptibilities are recorded [4,6,16]. In the image of Fig. 10d taken in a magnetic field of 4800 Oe, nearly all domain walls within the grains are removed and some grains show only small domains of reverse magnetization near the grain boundaries. (The maximum available field was too low to completely remove domain walls within the grains, and especially reverse domains.) As the external field was reduced, starting from these residual and newly formed reverse domains, predominantly near the grain boundaries of the larger grains, the magnetization reversal process was observed to proceed (often in an instantaneous way) by easy domain wall displacements (Fig. 10e–g). As a consequence, part of the grains was multidomain at the remanent state (Fig. 10g). Small grains are found to reverse their magnetization suddenly without forming stable domain walls and at larger reversed applied field (they have larger coercive forces) than the larger grains, as directly proved in Refs. [4,5] by observations using magneto-optic Kerr microscopy. With some exceptions, the magnetization reversal occurred independently in individual grains. Fig. 10g–l shows changes in the domain structure at the reversed external field, starting from the remanent state of Fig. 10g. They were similar in character to those observed previously (Fig. 10a–g).

The coercivity mechanism of sintered Nd–Fe–B-based magnets was considered to be determined either by the nucleation of reverse domains or the pinning of domain walls by inhomogeneities [66–68]. Distinctions between these two possibilities were studied in relation to the initial susceptibility behavior, domain structure, microstructure, and the dependence of coercivity on magnetizing field, temperature and the angle between the applied field and the alignment direction. The literature on this subject is often perplexing, and its terminology somewhat less than precise, in part because of the phenomenological and model-dependent nature of the criteria and also because the two mechanisms are not mutually exclusive [67]. Moreover, it is very difficult to distinguish experimentally between the nucleation and pinning nature of inhomogeneities at the grain boundaries [66,67,69]. At present, however, it

appears to be generally accepted that the coercivity of sintered Nd–Fe–B-based magnets is controlled mainly by the nucleation of reverse domains and consequently they are referred to as nucleation-type magnets. But domain wall pinning at the grain boundaries also plays a role, namely, it is required to prevent magnetization reversal of the whole magnet from a single weak nucleation site [66,67].

The experimental data reported in the literature indicate that often the reversal of magnetization is not a simple one-step process, but more complex process, involving different mechanisms [70,71]. In the context of the considered sintered Nd–Fe–B-based magnets, it is interesting to note that recent in situ TEM magnetizing experiments show that first the reversible process of nucleation and growth of reverse dipole domains predominantly in misaligned grains takes place (as the applied field is decreased slowly from positive saturation), and then the major irreversible process of nucleation and expansion of reverse domains starts to develop near the grain boundaries of well-aligned grains (as the applied field is further decreased and becomes negative) [69].

4. Conclusions

The magnetic structure of anisotropic sintered Nd–Fe–B-based permanent magnets of different chemical compositions has been investigated at the surfaces both perpendicular and parallel to the alignment axis. The techniques used were the conventional Bitter pattern method, the colloid-SEM technique, MFM and type-I magnetic contrast of SEM. As a result, useful complementary information on the magnetic domain structure could be obtained. The application of digital image recording, enhancement and analysis allowed to obtain domain images which have high contrast and show the details clearly, and to analyze them in detail. Improvements over earlier results were achieved.

In the thermally demagnetized state, nearly all grains show magnetic domains. At the surface perpendicular to the alignment axis, maze (main) domains of typically 1–2 μm wide and surface reverse spike domains of typically 0.5–1 μm in diameter were observed. This coarse domain structure is characteristic of sufficiently thick uniaxial crystals with high magnetocrystalline anisotropy, and was commonly reported in the past. However, MFM investigations show that, in addition to the coarse domains, a previously unobserved fine surface domain pattern is present. The fine surface domains had widths in the range 20–250 nm. They are found to be magnetized perpendicular to the specimen surface and their existence is attributed to the reduction of the magnetostatic energy near the surface.

The main and surface domain widths of the relatively complicated domain structure of the studied magnets were determined using the stereologic method of Bodenberger and Hubert. This was done by digital means, in contrast to studies carried out in the past. In this respect, it should be noted that determining the domain widths with the use of digital procedure includes much larger statistics and certainly is much more objective and precise than in the case of visual method. On the basis of the main domain widths, the domain wall energies of the investigated magnets were determined using the theory of Kaczér, the theory of Hubert and the extended theory of Szymczak. The mentioned theories were compared using the experimental data from the literature. To the author's knowledge, such a comparison has not been made previously. The comparison shows that the predictions of the extended theory of Szymczak are closest to the experiment. Using the domain wall energies obtained from the mentioned theory, other intrinsic parameters were also determined for the studied magnets.

For the basic Nd–Fe–B compound (specimens A, where the hard magnetic $Nd_2Fe_{14}B$ phase is present, not modified by additions of other elements), the domain wall energy was found to be (27 ± 4) erg/cm^2. This result is very close to the values 30 erg/cm^2 of Refs. [5,10], 24 erg/cm^2 of Refs. [7,11] and 25 erg/cm^2 of Ref. [9]. Nevertheless, it is to be noted that, as far as the author is aware, the domain wall energy of Nd–Fe–B-based compound (thus, in particular, of the basic Nd–Fe–B compound) has not yet been determined using sufficiently thin crystals (thinner than 10 μm), where the Kittel's parallel-plate domain structure occurs (to a very good approximation) and Eq. (2) can be applied. Note also that the domain wall energies increased with increasing Dy concentration.

Investigations of the behavior of the magnetic domain structure under the influence of an external magnetic field, conducted on the surface parallel to the alignment axis, show that the domain walls are easily moved within the grains and that the magnetization reversal process is predominantly related to the nucleation and growth of domains of reverse magnetization at structural imperfections near the grain boundaries.

Some aspects related to magnetic domain observation by the methods used were also presented and discussed. In particular, it was demonstrated that application of the conventional Bitter pattern technique for studying complex or relatively complex domain structures which exhibit domains comparable in size to the spatial resolution of the technique is in fact dangerous and may lead to incorrect results. Of all the methods applied in the presented investigations, MFM in the dynamic mode of operation is found to possess the best spatial resolution and the best surface sensitivity.

References

[1] J.M.D. Coey, J. Magn. Magn. Mater. 248 (2002) 441.
[2] D. Brown, B.M. Ma, Z. Chen, J. Magn. Magn. Mater. 248 (2002) 432.
[3] J.D. Livingston, J. Appl. Phys. 57 (1985) 4137.
[4] D. Li, K.J. Strnat, J. Appl. Phys. 57 (1985) 4143.
[5] M. Sagawa, S. Fujimura, H. Yamamoto, Y. Matsuura, S. Hirosawa, K. Hiraga, in: Proceedings of the Fourth International Symposium on Magnetic Anisotropy and Coercivity in Rare Earth-Transition Metal Alloys, Dayton, 1985, p. 587.
[6] T. Zhao, H. Jin, J. Deng, F. Wu, J. Song, Y. Shi, J. Magn. Magn. Mater. 54–57 (1986) 573.
[7] K.-D. Durst, H. Kronmüller, J. Magn. Magn. Mater. 59 (1986) 86.
[8] R. Szymczak, H. Szymczak, E. Burzo, IEEE Trans. Magn. 23 (1987) 2536.
[9] R. Szymczak, D. Givord, H.S. Li, Acta Phys. Pol. A 72 (1987) 113.
[10] Y. Luo, Q.G. Ji, N. Zhang, B.S. Han, J. Phys. C (Paris) 8 (1988) 589.
[11] J. Pastushenkov, A. Forkl, H. Kronmüller, J. Magn. Magn. Mater. 101 (1991) 363.
[12] D. Płusa, J.J. Wysłocki, B. Wysłocki, R. Pfranger, Appl. Phys. A 40 (1986) 167.
[13] D. Płusa, J.J. Wysłocki, B. Wysłocki, R. Pfranger, J. Less-Common Met. 133 (1987) 231.
[14] W.D. Corner, M.J. Hawton, J. Magn. Magn. Mater. 72 (1988) 59.
[15] T. Suzuki, K. Hiraga, M. Sagawa, Jpn. J. Appl. Phys. 23 (1984) L421.
[16] G.C. Hadjipanayis, K.R. Lawless, R.C. Dickerson, J. Appl. Phys. 57 (1985) 4097.
[17] R.K. Mishra, R.W. Lee, Appl. Phys. Lett. 48 (1986) 733.
[18] S. Young, J.N. Chapman, IEEE Trans. Magn. 29 (1993) 2779.
[19] M.A. Al-Khafaji, W.M. Rainforth, M.R.J. Gibbs, J.E.L. Bishop, H.A. Davies, IEEE Trans. Magn. 32 (1996) 4138.
[20] L. Folks, R.C. Woodward, J. Magn. Magn. Mater. 190 (1998) 28.
[21] E. Zueco, W. Rave, R. Schäfer, A. Hubert, L. Schultz, J. Magn. Magn. Mater. 190 (1998) 42.
[22] D.C. Crew, L.H. Lewis, V. Panchanathan, J. Magn. Magn. Mater. 231 (2001) 57.
[23] M. Sagawa, S. Fujimura, H. Yamamoto, Y. Matsuura, K. Hiraga, IEEE Trans. Magn. 20 (1984) 1584.
[24] K. Hiraga, M. Hirabayashi, M. Sagawa, Y. Matsuura, Jpn. J. Appl. Phys. 24 (1985) 699.
[25] K. Makita, O. Yamashita, Appl. Phys. Lett. 74 (1999) 2056.
[26] W. Szmaja, J. Magn. Magn. Mater. 189 (1998) 353.
[27] F. Bitter, Phys. Rev. 38 (1931) 1903.
[28] K. Goto, T. Sakurai, Appl. Phys. Lett. 30 (1977) 355.
[29] R. Carey, E.D. Isaac, Magnetic Domains and Techniques for Their Observation, Academic Press, New York, 1966 (p. 48).
[30] P. Grütter, H.J. Mamin, D. Rugar, in: R. Wiesendanger, H.-J. Güntherodt (Eds.), Scanning Tunneling Microscopy II, Springer, Berlin, 1992 (p. 151).
[31] U. Hartmann, Annu. Rev. Mater. Sci. 29 (1999) 53.
[32] D.C. Joy, J.P. Jakubovics, Br. J. Appl. Phys. (J. Phys. D) 2 (1969) 1367.
[33] W. Szmaja, J. Magn. Magn. Mater. 202 (1999) 201.
[34] W. Szmaja, Phys. Status Solidi A 194 (2002) 315.
[35] W. Szmaja, Czech. J. Phys. 54 (2004) 1503.
[36] R.J. Celotta, J. Unguris, M.H. Kelley, D.T. Pierce, Methods in Materials Research: a Current Protocols Publication, Wiley, New York, 2000 (Unit 6b.3).
[37] U. Hartmann, J. Magn. Magn. Mater. 68 (1987) 298.
[38] J. Šimšová, R. Gemperle, J.C. Lodder, J. Magn. Magn. Mater. 95 (1991) 85.
[39] T. Sakurai, O. Kitakami, Y. Shimada, J. Magn. Magn. Mater. 130 (1994) 384.
[40] W. Szmaja, J. Grobelny, M. Cichomski, K. Makita, W. Rodewald, Phys. Status Solidi A 201 (2004) 550.
[41] M.A. Al-Khafaji, W.M. Rainforth, M.R.J. Gibbs, J.E.L. Bishop, H.A. Davies, J. Appl. Phys. 83 (1998) 6411.
[42] W. Szmaja, J. Grobelny, M. Cichomski, K. Makita, Vacuum 74 (2004) 297.
[43] W. Szmaja, J. Grobelny, M. Cichomski, Appl. Phys. Lett. 85 (2004) 2878.
[44] W. Szmaja, J. Magn. Magn. Mater. 219 (2000) 281.
[45] W. Szmaja, J. Electron Spectrosc. Relat. Phenom. 148 (2005) 123.
[46] J.B. Goodenough, Phys. Rev. 102 (1956) 356.
[47] P. Thompson, O. Gutfleisch, J.N. Chapman, I.R. Harris, J. Magn. Magn. Mater. 202 (1999) 53.
[48] W. Rodewald, M. Katter, B. Wall, R. Blank, G.W. Reppel, H.D. Zilg, IEEE Trans. Magn. 36 (2000) 3279.
[49] R. Bodenberger, A. Hubert, Phys. Status Solidi A 44 (1977) K7 (in German).
[50] A. Hubert, R. Schäfer, Magnetic Domains: the Analysis of Magnetic Microstructures, Springer, Berlin, 1998 (pp. 329, 386, 550).
[51] C. Kittel, Phys. Rev. 70 (1946) 965.
[52] C. Kooy, U. Enz, Philips Res. Rep. 15 (1960) 7.
[53] R. Szymczak, Electron Technol. 1 (1968) 5.
[54] R. Szymczak, J. Appl. Phys. 39 (1968) 875.
[55] J. Kaczér, Zh. Eksp. Teor. Fiz. 46 (1964) 1787 (in Russian); J. Kaczér, Sov. Phys. JETP 19 (1964) 1204.
[56] A. Hubert, Phys. Status Solidi 24 (1967) 669 (in German).
[57] R. Szymczak, Acta Phys. Pol. A 43 (1973) 571.
[58] G.S. Kandaurova, Izv. Vyssh. Utchebn. Zaved. Fiz. 5 (1964) 12 (in Russian).
[59] K. Goto, Jpn. J. Appl. Phys. 5 (1966) 117.
[60] E.D. Isaac, Proc. Phys. Soc. 74 (1959) 786.
[61] J. Kaczér, R. Gemperle, Czech. J. Phys. B 10 (1960) 505.
[62] M. Rosenberg, C. Tănăsoiu, V. Florescu, J. Appl. Phys. 37 (1966) 3826.
[63] J.D. Livingston, M.D. McConnell, J. Appl. Phys. 43 (1972) 4756.
[64] D. Płusa, R. Pfranger, B. Wysłocki, Phys. Status Solidi A 92 (1985) 533.
[65] M. Sagawa, S. Hirosawa, K. Tokuhara, H. Yamamoto, S. Fujimura, Y. Tsubokawa, R. Shimizu, J. Appl. Phys. 61 (1987) 3559.
[66] G.C. Hadjipanayis, in: J.M.D. Coey (Ed.), Rare-Earth Iron Permanent Magnets, Clarendon Press, Oxford, 1996 (p. 286).
[67] J.F. Herbst, Rev. Mod. Phys. 63 (1991) 819.
[68] E. Burzo, Rep. Prog. Phys. 61 (1998) 1099.
[69] V.V. Volkov, Y. Zhu, J. Magn. Magn. Mater. 214 (2000) 204.
[70] C. Daboo, R.J. Hicken, E. Gu, M. Gester, S.J. Gray, D.E.P. Eley, E. Ahmad, J.A.C. Bland, R. Ploessl, J.N. Chapman, Phys. Rev. B 51 (1995) 15964.
[71] J.N. Chapman, P.R. Aitchison, K.J. Kirk, S. McVitie, J.C.S. Kools, M.F. Gillies, J. Appl. Phys. 83 (1998) 5321.